Peer reviewed version

University of Bristol - Explore Bristol Research
General rights

Aeroacoustic Performance of High-lift Airfoil with Serrated Slat Cusp

Hasan Kamliya Jawahar[*],
University of Bristol, Bristol, United Kingdom, BS8 1TR
Syamir Alihan Showkat Ali[†],
Universiti Malaysia Perlis, 02600, Perlis, Malaysia
Mahdi Azarpeyvand[‡],
University of Bristol, Bristol, United Kingdom, BS8 1TR
and
Carlos R. Ilário da Silva[§]
Embraer, São José dos Campos, 12227-901, Brazil

Experimental measurements to assess the aeroacoustic capabilities of 30P30N airfoil fitted with two different types of serrated slat cusps were carried out at the aeroacoustic wind tunnel at the University of Bristol. The results from the simultaneous surface pressure measurement within and close to the slat cove region and far-field noise measurements above the slat trailing edge are presented to gain a deeper understanding of the noise generation mechanism of the slat and other presented configurations. The far-field noise measurement results showed that significant noise reduction at the vortex shedding frequency can be achieved by the use of serration-2 and No-Cusp configuration. The coherence results for all the frequencies are almost zero for the No-Cusp configuration and the coherence was notably reduced for the Serration-2 configuration. Further higher order statistical and spectral analysis showed that even the serration-1 with small serrations reduces the energy within the norrowband peaks to some level.

Nomenclature

c	=	stowed chord length, m
c_s	=	slat chord length, m
C_L	=	lift coefficient
C_D	=	drag coefficient
C_p	=	pressure coefficient, $(\overline{p} - p_\infty)/(0.5\rho U_\infty^2)$
f	=	frequency, Hz
k	=	turbulent kinetic energy, $\mathrm{m^2/s^2}$
l	=	span length, m
$\overline{p}$	=	average pressure, Pa
p'	=	fluctuation surface pressure, Pa
P_{ref}	=	reference pressure ($= 2 \times 10^{-5}$), Pa
P_{rms}	=	pressure root mean squared
p_∞	=	static pressure of the flow, Pa
Re_c	=	chord-based Reynolds number
St_s	=	slat chord-based Strouhal number, $(St_s = f \cdot c_s/U_\infty)$
U, U_∞	=	mean velocity, freestream velocity, m/s
ρ	=	air density, $\mathrm{kg/m^3}$
α	=	angle of attack, °
τ	=	time delay, s
Φ_{pp}	=	wall-pressure power spectral density, $\mathrm{Pa^2/Hz}$
$\gamma^2_{p_i p_j}$	=	wall pressure coherence between transducers p_i and p_j
Λ_γ	=	spanwise coherence length, m

[*]Research Associate, Department of Aerospace Engineering, hasan.kj@bristol.ac.uk
[†]Senior Lecturer, School of Manufacturing Engineering, Universiti Malaysia Perlis, 02600, Perlis, Malaysia, syamir@unimap.edu.my
[‡]Professor in Aeroacoustics, Department of Mechanical Engineering, m.azarpeyvand@bristol.ac.uk
[§]Technology Development Engineer, Embraer, São José dos Campos, Brazil, carlos.ilario@embraer.com.br

I. Introduction

OVER the past decade, the boost in the commercial air travel has stipulated the aircraft industry to produce efficient and quieter aircraft than the ones already in use. With the use of high bypass engines, the noise generated by the engine has significantly been lowered, yet, the airframe noise remains unaltered. This airframe noise is extensively caused by landing gears and high-lift devices like the slats and flaps. Various passive and active flow control methods have shown to reduce these noise levels by the use morphing structures [1–6], porous materials [7–11], and serrations [12–18]. Nonetheless, conventional slat and wing configurations prove that slat noise majorly comprises of broadband and tonal noise components and in addition to this, studies have also shown several discrete tones at mid-frequency range [19–31]. The aeroacoustic mechanism used in these configurations is yet to be completely understood and interpreted. Slat noise reduction mechanisms that have proven successful are slat cove cover, slat hook extensions, slat cove filler, slat gap reduction, slat acoustic liners, slat hook tripping, slat hook serrations and slat trailing with porous or brush extensions [32].

One of the most definite ways of reducing the broadband noise generated from the slat cove region is by filling the recirculation area within the slat cove gap [33–43]. These tonal peaks in the slat are a result of vortex shedding at the slat cusp and impingement on the lower surface of the slat along with a feedback loop present in between them. Filling the slat cavity has shown to have eliminated this tonal noise and the broadband noise from the shear layer impingement. A very recent study by Jawahar *et al.* [2] reported the aerodynamic and aeroacoustic characteristics of slat cove fillers. The results indicated that the slat cove fillers do not adversely affect the aerodynamic performance of the wing. They also showed that the characteristic vortex shedding peak in the slat noise was eliminated with the use of slat cove fillers along with a noise reduction of up to 10 dB in the narrowband region and up to 3 dB in the broadband region.

Kopiev *et al.* [44] performed a parametric study using seven serrations with increasing serration wavelength. They showed that the serration with a smaller wavelength was sufficient enough for noise reduction with up to 8 dB for the narrow-band peak. The serrated slat hook with a smaller wavelength did not significantly affect the aerodynamic performance. The characteristic narrowband peaks were eliminated by the use of slat serrations. The parametric study also showed that serration with larger wavelength increased broadband noise and slightly degraded aerodynamic performance.

Even though Kopiev *et al.* [44] has shown overall noise reduction capabilities of slat serration the studies on the aerodynamic and aeroacoustic behavior of serrated slat cusp in the literature is lacking. This experimental study presents detailed aeroacoustic performance characteristics with high-quality aeroacoustic measurements acquired from the state of the art aeroacoustic facility at the University of Bristol. The acoustic results presented show a comprehensive analysis of the performance of 30P30N airfoil fitted with two types of serrated slat cusps.

II. Experimental Setup

A. Airfoil Setup

A 30P30N three-element high-lift airfoil was manufactured using a computer-aided numerically controlled machine with a retracted chord of $c = 0.35$ m and a span of $l = 0.53$ m. The airfoil was designed with no brackets within the test section to maintain two-dimensionality of the flow within the slat cove and flap cove regions. A rigid purpose-built steel clamp was used to hold the three-elements together from the airfoil sides. The slat was built with a slot to facilitate interchangeable slat leading-edge devices. A zig-zag turbulator tape (see Fig. 1) with a thickness of $h_t = 0.5$ mm and a width of $w_t = 6$ mm with a turbulator angle of 70° was used at location $x/c = -0.055$ on the pressure side of the slat surface just upstream of the slat cusp to trip the flow and induce turbulent shear layer [21]. The airfoil was also equipped with a large number of static pressure taps (103) placed along the mid-span of the airfoil for aerodynamic and aeroacoustic measurements. The tests were carried out for two different types of serrated slat cusp configuration. The specification of the two serration configuration used in the present study are detailed in Fig. 1 and shown in Fig. 1 and 2. The interchangeable slat leading-edge devices were manufactured using rapid prototyping.

Table 1. Geometrical parameters of slat cusp serrations.

Configuration	Serration Type	$2h$ (mm)	λ (mm)	λ/h -	α_s (deg.)
Serration 1	sawtooth	3.8	3.12	1.64	67.7
Serration 2	sawtooth	6.4	3.12	0.975	76.3

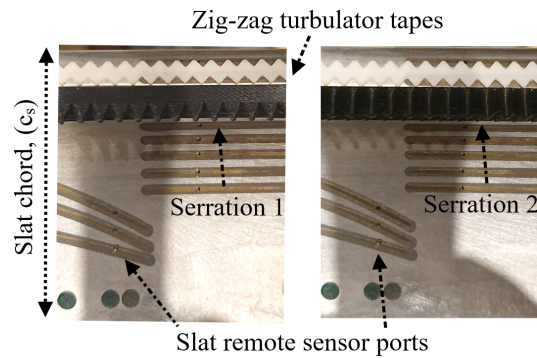American Institute of Aeronautics and Astronautics

Fig. 1. Close up view of the slat with serrated leading-edge inserts and zig-zag turbulators.
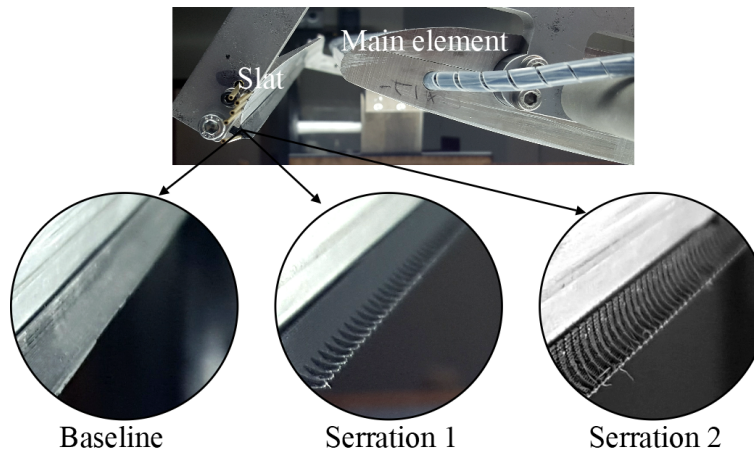

Fig. 2. The different slat configurations tested in the present study.

B. Wind-Tunnel Setup

The aerodynamic measurements were carried out in the large low-speed closed-circuit wind tunnel at the University of Bristol. It has an octagonal working area of 2.1 m × 1.5 m × 2 m and a contraction ratio of 3:1. The wind-tunnel is capable of a maximum velocity up to 60 m/s with typical turbulence intensity levels as low as 0.25%. The aeroacoustic measurements were carried out at the University of Bristol Aeroacoustic Facility. It is a closed circuit open-jet anechoic wind tunnel with a nozzle exit of 0.5 m × 0.775 m and a contraction ratio of 8.4:1. The wind tunnel is capable of velocities up to 40 m/s with turbulence levels as low as 0.25% [45].

1. Unsteady Pressure Measurements Setup

FG-3329-P07 transducers from Knowles Electronics were installed on the main-element of the wing to measure the unsteady surface pressure on the MDA airfoil (see Table. 2). This transducer was selected for measurement as it was proven successful in previous experiments carried out by Garcia [46–48] on NACA 0012 airfoil. The transducer has a diameter of 2.5 mm and a height of 2.5 mm with a sensing area of 0.8 mm. The FG-3329-P07 transducer has manufacturer-provided sensitivity of 22.4 mV/Pa (45 Pa/V) in the flat region of the transducer response. The transducer sensitivity obtained from the calibration varied between 20.2 mV/Pa and 23.5 mV/Pa. The unsteady surface pressure measurements using FG transducers were carried out for 16 seconds using a sampling frequency of $f = 2^{16}$ Hz.

The unsteady surface pressure measurements were also performed using the remote sensors (M1-M4, S1), which were installed on the main-element and the slat of the wing, see Table. 2. The remote sensors comprised of a brass pipe fitted in a designated slot on the surface of a metal base. The Panasonic WM-61A miniature microphone is placed in between of a metal section and the metal base. Another drilled pinhole connecting to the surface of the brass pipe was aligned with the center of the microphone's pinhole. A flexible tube extension is connected to the other end of the brass pipe for anechoic termination. The calibration of the remote sensor produced the transfer functions required to

American Institute of Aeronautics and Astronautics

compensate for the dissipative effects and the lag produced by the remote sensors extensions. The measurements can be made up to a frequency of 9 kHz.
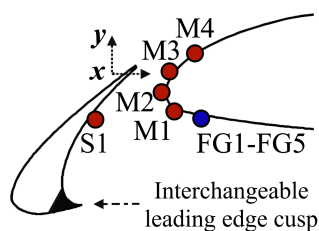

Fig. 3. Location of the remote unsteady pressure measurement probes (red) and flush mounted pressure transducers (blue).

Table 2. Streamwise and spanwise unsteady pressure measurement location on the main-element and slat for the 30P-30N high-lift airfoil.

No.	x (mm)	y (mm)	z (mm)
S1	-6.918	-11.622	265
M1	17.347	-10.019	265
M2	15.126	-5.839	265
M3	17.622	0	265
M4	23.520	5.485	265
FG1	22.414	-11.356	277
FG2	22.414	-11.356	280.6
FG3	22.414	-11.356	288.4
FG4	22.414	-11.356	301.4
FG5	22.414	-11.356	319.6

2.   Acoustic measurements and instrumentation

The far-field noise measurements were carried out using a Panasonic WM-61A electret microphone placed at a distance of 1 m, 90° from the trailing edge of the slat. The Panasonic WM-61A electret microphone has a flat frequency response at frequencies from 50 Hz to 10 kHz, with a dynamic range of more than 62 dB. The diameter of the exposed microphone diaphragm of the WM-61A microphones is 2 mm. The far-field noise data were captured for $t = 16$ s at a sampling frequency of $f = 2^{15}$ Hz. The acoustic data were recorded at a flow velocity of 30 m/s. The power spectrum results were obtained using the power spectral density (PSD) of the pressure signals with the Hanning window and the acquired data were averaged for 200 times to yield a frequency resolution of $\Delta f = 6.25$ Hz. The sound pressure level (SPL) spectrum can then be calculated from $SPL = 20 \cdot log_{10}(p_{rms}/p_{ref})$, where p_{rms} is the root-mean-square of the acoustic pressure and $p_{ref} = 20\ \mu$Pa is the reference pressure. The SPL of the acoustic pressure signal for the far-field measurement is corrected to a reference distance of 1 m.

III.   Results and Discussion

A.   Far-field spectral levels

The far-field noise measurements were carried out in order to investigate the noise generated from the Baseline, Serration-1 (Ser-1), Serration-2 (Ser-2), and No-Cusp configurations. The sound pressure level measured from a far-field microphone at 90° above the slat trailing edge for the angle of attack $\alpha = 14°$ and $18°$ at the free-stream velocity of $U_\infty = 30$ m/s is shown in Fig. 4. The sound pressure levels are presented in terms of the slat based Strauhal number ($St_s = f \times c_s/U_\infty$). The results for the Baseline and Ser-1 configuration of the 30P30N airfoil show the discrete narrowband peaks, particularly at $St_s = 1.6$, typical of the noise signature from such high lift devices. However, the far-field noise results of the Ser-2 and No-Cusp configuration do not demonstrate such tonal behavior. The Ser-1 configuration at the angle of attack $\alpha = 14°$ clearly shows a reduction in the noise levels at $St_s = 1.6$ and on the contrary, the noise level increases at the angle of attack $\alpha = 18°$ at $St_s = 1.6$. It can be observed that there is a slight shift in the Strouhal number (i.e., shifted to a lower St_s number) in the case of the Ser-1 compared to that of the main

peak seen in the Baseline configuration. Significant noise reduction at $St_s = 1.6$ can be seen in the case of Ser-2 and No-Cusp compared to that of the Baseline and Ser-1 cases. The results have also shown that the noise level increases at low to mid-frequency range ($St_s < 2$) for the Ser-1, Ser-2 and No-Cusp configurations and remain similar at high frequencies ($St_s > 2$) for both the angles of attack, $\alpha = 14°$ and $\alpha = 18°$. The generation of the tonal peaks and the mechanisms driving them will be discussed in detail in the following sections.
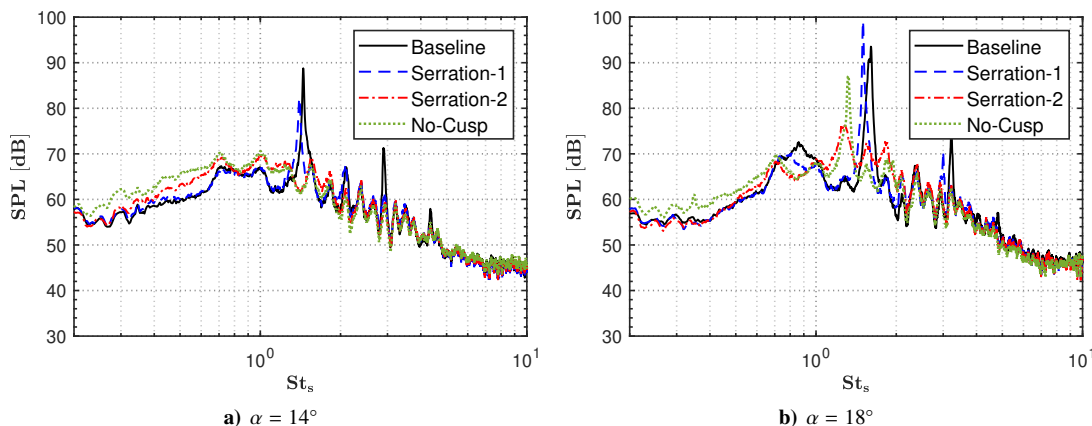

a) $\alpha = 14°$ **b)** $\alpha = 18°$

Fig. 4. Far-field noise spectra for microphone at $90°$ **and 1 m above the slat trailing edge.**

B.   Near-field spectral levels

In order to gain an insight into the noise generation mechanism of the slat, the near-field unsteady pressure measurements were carried out. The unsteady surface pressure measurements were acquired at various spanwise locations on the surface of the main-element and slat of the high-lift airfoil. The measurements were carried out using 5 surface-mounted pressure transducers, which are detailed in Table 2. The measurements were carried out for the angles of attack 14° and 18°. The results from the unsteady surface pressure measurements from the transducer FG1 at the leading-edge of the main-element are shown in Fig. 5. The tonal characteristics of the wall pressure spectra indicate the presence of cavity oscillations [2]. The wall pressure fluctuation spectra results for the Baseline in Fig. 5 show multiple distinct narrowband peaks for all the tested angles of attack with varying intensities, characterizing cavity oscillations. Some of the tonal peaks could also observed in the far-field noise measurements at a distance of 1 m away form the slat trailing edge. A similar trend could also be seen in the case of Ser-1. Compared to the Baseline case the Ser-1 possesses a slight reduction at the vortex shedding peak ($St_s = 1.6$) for the angle of attack $\alpha = 14°$ and increased levels for the same peak at the angle of attack $\alpha = 18°$. It appears that the wall pressure spectra at the angle of attack $\alpha = 14°$, for the Ser-2 and No-Cusp, show an increase of sound pressure level over the whole frequency range and an increase of sound pressure level in the low-mid frequency range at the angle of attack $\alpha = 18°$. The increased spectral levels at high frequencies ($St_s > 3$) seen in the near-field surface pressure measurements for the Ser-2 and No-Cusp configurations are absent in the far-field measurements in Fig.4 for the angle of attack $\alpha = 14°$, which implies that the increased spectra in the near-field are due to the non-propagating hydrodynamic energy field within the slat and main-element. The results for the Ser-2 evidently show that the characteristic narrow band peak from the slat noise is eliminated. However, in the case of No-Cusp the narrowband peaks are observed but with a much reduced tonal intensity.

The results for the unsteady surface pressure measurements from the remote pressure transducer M1-M4 on the main-element and S1 on the slat are shown in Fig. 6. The wall pressure fluctuation spectra results for the Baseline case show multiple distinct narrowband peaks for all the tested angles of attack with varying intensities, indicating the presence of cavity oscillations. Similar tonal peaks can also be observed in the far-field noise measurements, see Fig. 4. Some of the discrete narrowband peaks seen at high-frequency of the Baseline and Ser-1 cases were not seen in the Ser-2 and No-Cusp configurations. The transducer S1 exhibits the lowest sound pressure level compared to that of the transducers (M1-M4) at the leading-edge of the main-element for all the configurations tested (i.e., Baseline, Ser-1, Ser-2, and No-Cusp). The presence of the spectral hump is observed in the case of Baseline $St_s = 0.6$ at the angles of attack $\alpha = 14°$ and $\alpha = 18°$. The results for the Ser-2 and No-Cusp cases at the angle of attack $\alpha = 14°$ show that the spectral hump has been completely eliminated, however, at the angle of attack $\alpha = 18°$, a spectral hump ($St_s = 0.6$) similar to that of the Baseline is observed. Note that the broadband hump in this region might be different
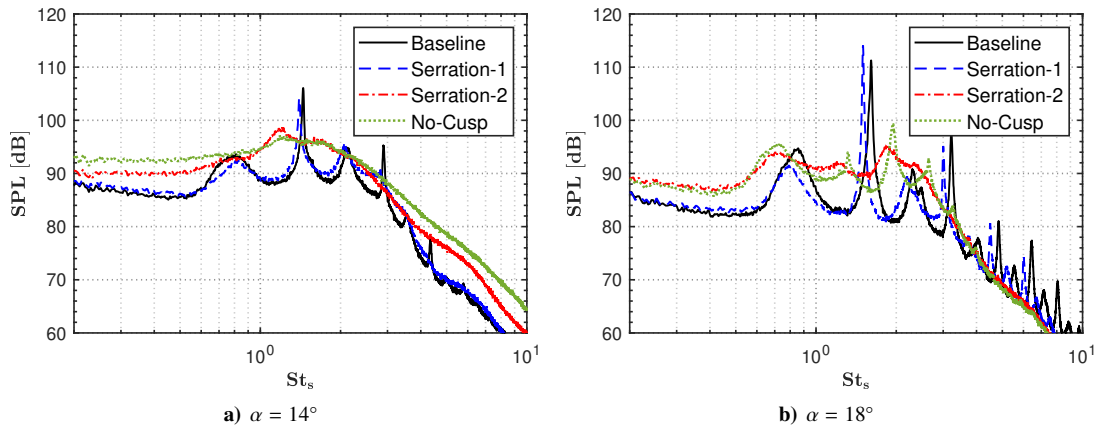
a) $\alpha = 14°$

b) $\alpha = 18°$

Fig. 5. Near-field noise spectra for flush mounted surface pressure transducer (FG1) at the leading-edge of the main-element.

in nature compared to the dominant even-numbered modes seen in the Baseline case. The results also show that the Ser-2 and No-Cusp cases can significantly reduce or eliminate the vortex shedding peak at $St_s = 1.6$, particularly at the angle of attack $\alpha = 14°$. The multiple narrowband peaks are completely eliminated for angle of attack $\alpha = 14°$ for both Ser-2 and No-Cusp configurations. Interestingly, at the angle angle of attack $\alpha = 18°$, the narrowband peaks are just eliminated for the Ser-2 but not for the No-Cusp configuration.

a) **Baseline,** $\alpha = 14°$

b) **Baseline,** $\alpha = 18°$

c) **Serration 1,** $\alpha = 14°$

d) **Serration 1,** $\alpha = 18°$

e) **Serration 2,** $\alpha = 14°$

f) **Serration 2,** $\alpha = 18°$

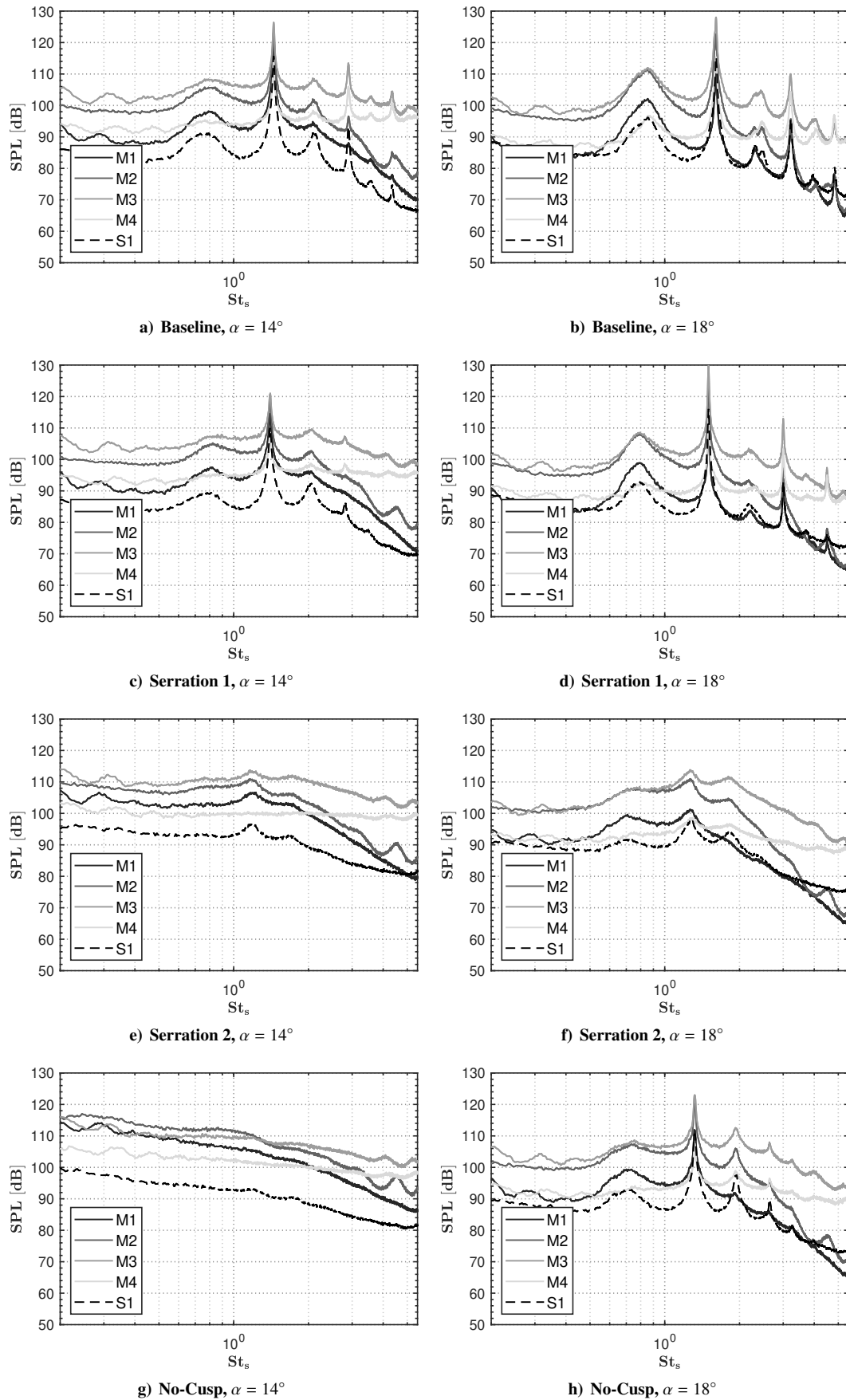g) **No-Cusp,** $\alpha = 14°$

h) **No-Cusp,** $\alpha = 18°$

Fig. 6. Comparison of the near-field noise spectra for the surface remote sensors (M1-M4, S1) on the main element and the slat of the wing.

American Institute of Aeronautics and Astronautics

C. Statistical Analysis

In order to characterize the turbulent motions of the high-lift airfoil with and without the serrated slat cusp, the statistical moments of the turbulence distribution are studied using skewness and kurtosis. The results of the skewness and kurtosis for the Baseline, Ser-1, Ser-2, and No-Cusp configurations at the angle of attack 14° and 18° are presented in Fig. 7. The skewness measures the asymmetry of the data signal distribution around the sample mean. The data exhibits a Gaussian distribution if the skewness value is between -0.5 and 0.5. The results show that the skewness for all the configurations is within or close to the limits of a Gaussian distribution, except for the transducer M4 in the case of the Baseline configuration. The skewness of the pressure events at M4 is lower than -0.5 for the Baseline case, indicating that the size of the left-handed tail is larger than the right-handed tail of the distribution. The kurtosis, on the other hand, measures whether the data are peaked or flat relative to the normal distribution. The data exhibits a Gaussian distribution if the kurtosis of the normal distribution is 3. The results clearly show that all the cases have kurtosis value below 3 for the pressure transducers M1, M2, and M3 except for the No-Cusp case (M3), signifying the occurrence of platykurtic distribution with fewer values in the tails and close to the mean. The results obtained could be possibly related to the presence of the persistence turbulence associated with the peak on the near field spectral analysis observed in Fig. 6. The kurtosis value measured at transducer M4 shows higher kurtosis value, which tends to have a distinct peak near the mean with heavy tails. Further analysis is needed to better understand the relationship between the statistical results of the skewness and kurtosis and the flow characteristics over the vicinity of the airfoil.
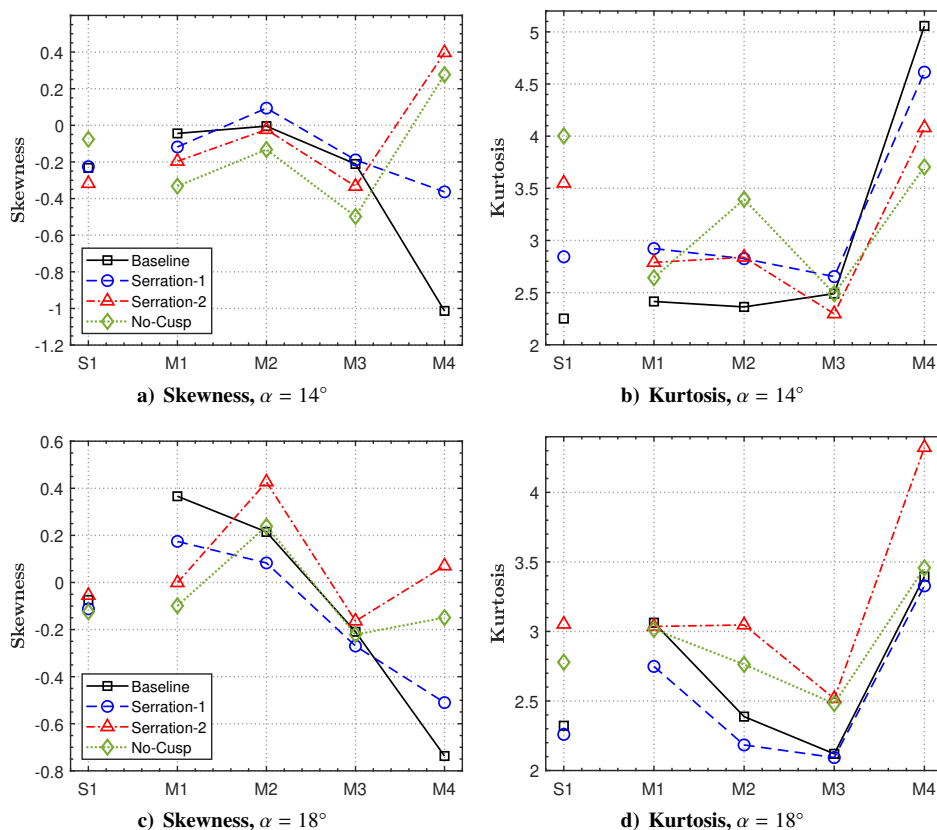

Fig. 7. Skewness and Kurtosis at various remote sensor on the main-element show in Fig. 3.

D. Coherence studies

To better understand the hydrodynamic field and radiated noise, the coherence between the two different pressure transducers at the slat and the leading-edge of the main-element were studied. The coherence between the near-field pressure transducers and the far-field microphone were also carried out. The coherence between the surface pressure transducers was calculated using the following equation,

$$\gamma^2_{p_i p_j}(f) = \frac{\mid \Phi_{p_i p_j}(f) \mid^2}{\Phi_{p_i p_i}(f)\Phi_{p_j p_j}(f)}, \tag{1}$$

where p_i is the reference pressure transducer and p_j is the unsteady pressure transducers mounted at the slat and the leading-edge of the main-element and the far-field microphone placed at 90°, 1 m above the slat trailing-edge.

1. Near-field coherence studies

The coherence between the reference transducer M1 and the other surface transducers M2, M3 and M4, for Baseline, Ser-1, Ser-2, and No-Cusp configurations are presented in Fig. 8. The results show high coherence in the case of the coherence between the M1 and M2 pressure transducers for all the cases at both the angles of attack over the whole frequency range. The coherence results for the transducers with the largest streamwise spacing between M1 and M4 show reduction in the coherence level for all the cases at both the angles of attack, with a significant reduction of the coherence level at almost zero can be seen in the case of Ser-2 and No-Cusp configurations at the angle of attack $\alpha = 14°$. The results show a high level of coherence at $St_s = 0.6$, indicating the emergence of spectral hump for all the presented cases and all configurations. Interestingly, a high level of coherence for the broadband spectral hump at low frequencies was significantly reduced for both the Ser-2 and No-Cusp configurations especially at the angle of attack $\alpha = 14°$. The results also show that a high level of coherence can be seen at the vortex shedding peak ($St_s = 1.6$) for all the cases at both the angles of attack except for the Ser-2 and No-Cusp cases at the angle of attack $\alpha = 14°$. The coherence results at the vortex shedding peak at $St_s = 1.6$ is almost zero for the No-Cusp configuration and the coherence was notably reduced for the Ser-2 configuration, which is consistent with the results observed in the surface pressure spectra in Figs. 5 and 6 for angle of attack $\alpha = 14°$. The results have also shown that at the angle of attack $\alpha = 18°$, the coherence level decays quickly in the streamwise direction and ratifies that after the maximum ($St_s = 1.6$), the coherence of the peak seems to sharply decay in a decreasing trend with microphone distance at $St_s = 2$. The coherence results at the angle of attack $\alpha = 18°$ show that except for the tonal peaks, the emergence of another spectral hump can be seen at high frequencies (between $St_s = 3$-$St_s = 5$) for the Baseline, Ser-1, and Ser-2 cases. The broadband hump in this region might be different in nature and further research is needed to address this issue.

2. Far-field coherence studies

Figure 9 shows the coherence $\gamma^2_{p_i p_{90°}}$ between the near-field surface pressure transducers on the slat and the main-element of the high-lift airfoil (S1, M1-M4) and the far-field microphone (FF1) for the Baseline, Ser-1, Ser-2 and No-Cusp configurations. The far-field microphone is placed at 90° above the slat trailing-edge, with a reference distance of 1 m. The results show a high coherence level in the case of the coherence between the FF1 microphone and S1 pressure transducer and low coherence level between the FF1 microphone and M4 pressure transducer for all the cases at both the angles of attack over the whole frequency range. The near- to far-field results show high coherence at all tonal peaks that appear due to the Rossiter modes from the presence of cavity oscillations [2]. It can be seen that a high level of coherence for the broadband hump at about $0.5 < St_s < 0.9$ and the vortex shedding peak at $St_s = 1.6$ can be significantly reduced with the application of Ser-2 for both angles of attack. The coherence of the broadband hump, the vortex shedding peak and the other distinct narrowband peaks observed in the Baseline case can be completely eliminated with the No-Cusp configuration with the coherence values below $\gamma^2_{p_i p_{90°}} > 0.1$, particularly at the angle of attack $\alpha = 14°$, which is consistent with the results observed in Figs. 4, 5 and 6.

a) **Baseline,** $\alpha = 14°$

b) **Baseline,** $\alpha = 18°$

c) **Serration 1,** $\alpha = 14°$

d) **Serration 1,** $\alpha = 18°$

e) **Serration 2,** $\alpha = 14°$

f) **Serration 2,** $\alpha = 18°$

g) **No-Cusp,** $\alpha = 14°$
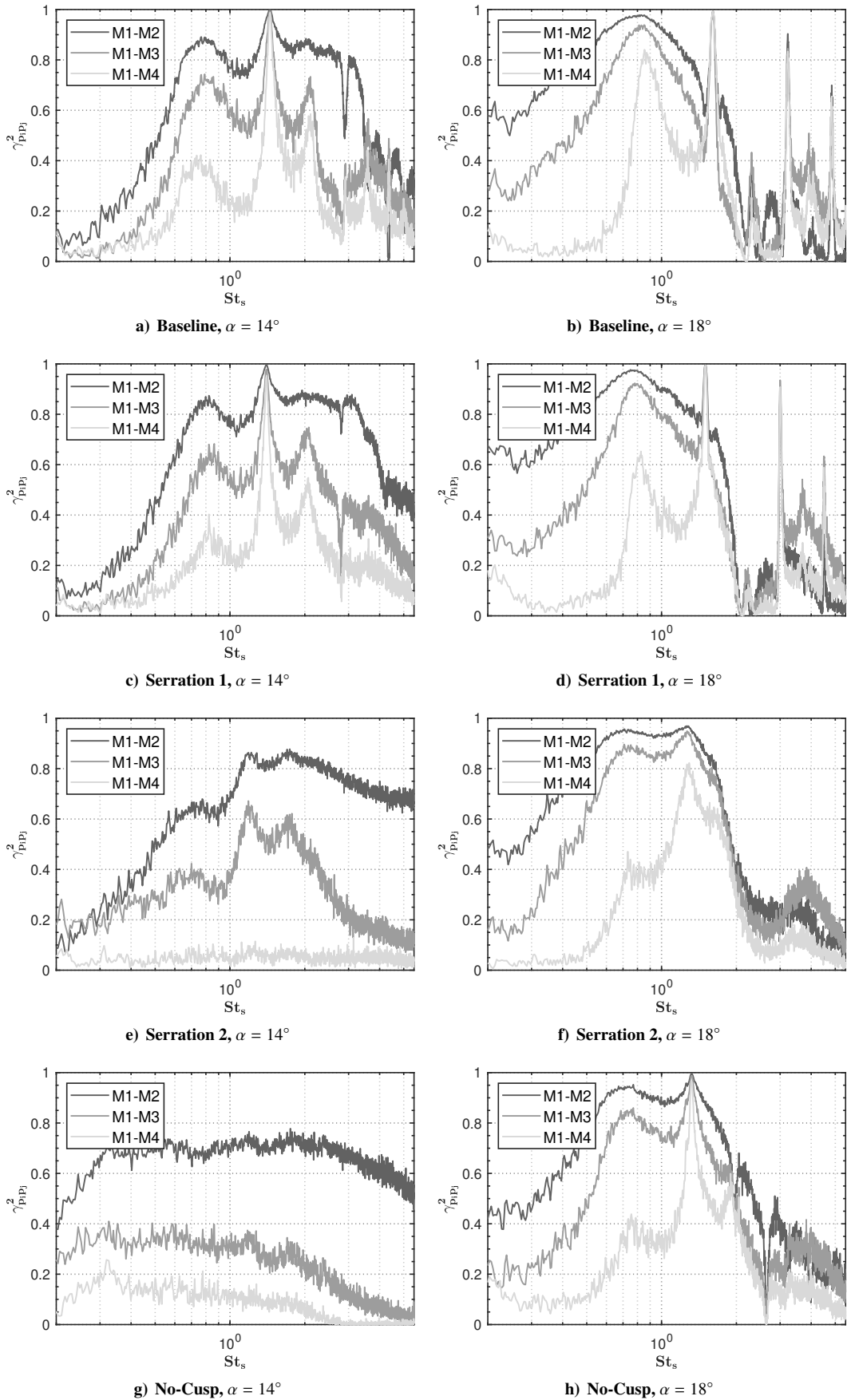
h) **No-Cusp,** $\alpha = 18°$

Fig. 8. Coherence between the surface pressure transducers on the main-element with M1 as the reference signal.
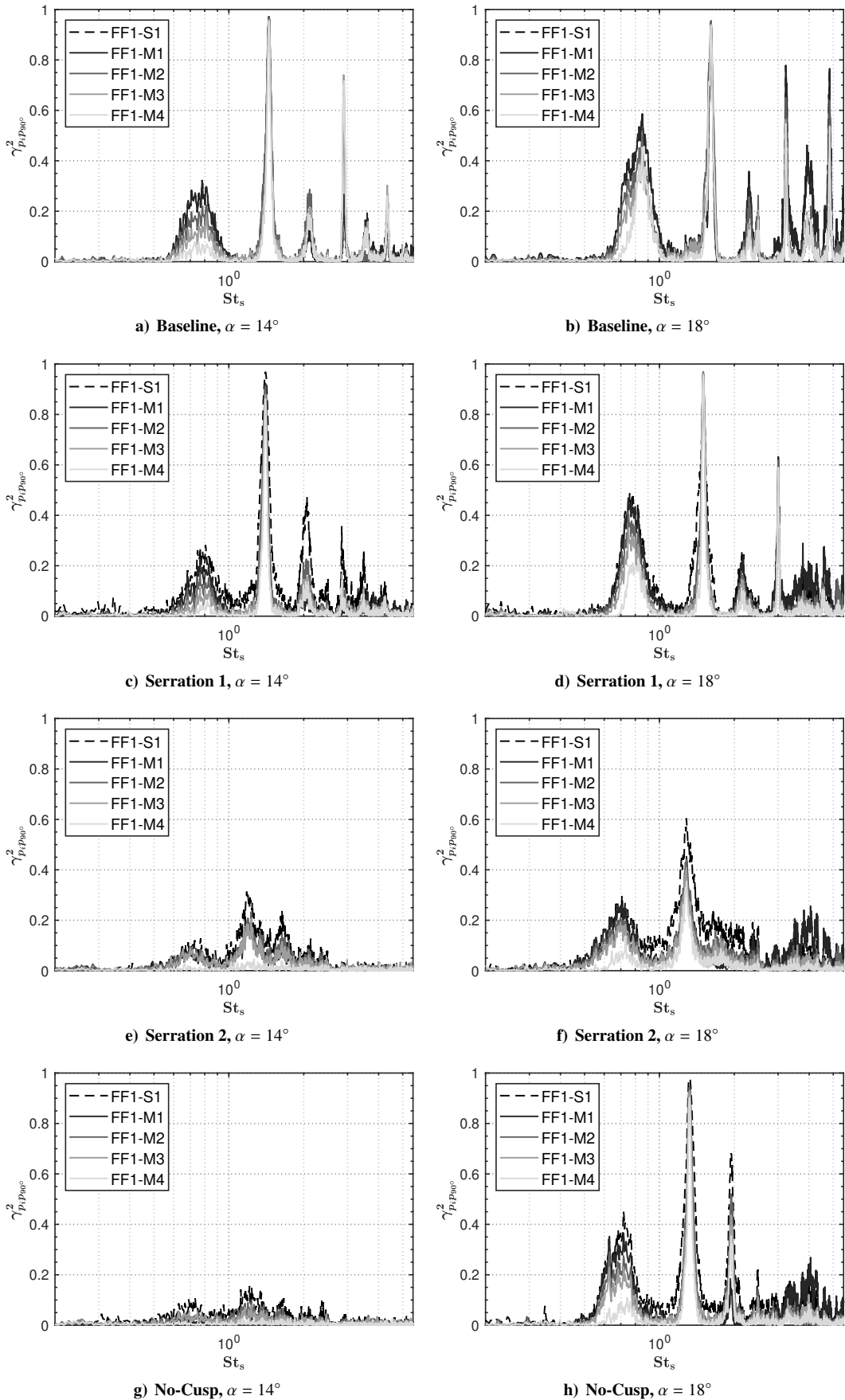
Fig. 9. Coherence between the far-field microphone at 1 m above the trailing edge and surface pressure transducers on the high-lift airfoil.

E. Continuous wavelet transform

In order to better understand the temporal characteristics of the pressure signals and their associated frequency, the continuous wavelet transform (CWT) method [2] has been employed in the present study. The contour plots of the wavelet coefficient magnitude of the surface pressure signal of the transducer M1 for the Baseline, Ser-1, Ser-2, and No-Cusp configurations at the angle of attack 18° are presented in Fig. 10. The measurements were performed for $16\ s$ and the results are presented for $0.6\ s$ for better visualization. For the Baseline case, it is apparent that the temporal characteristics of the signal exhibit amplitude modulation in time for the first three peaks observed in Fig. 5(b). The results show that the highest level of energy in the time-frequency domain is dominated by the peak at $St_s = 1.6$, corresponding to the vortex shedding frequency. A similar observation can be seen in the case of Ser-1, with a slight shift of the fundamental vortex shedding peak to a lower frequency region. For Ser-2 and No-Cusp configurations, the results clearly show increasing occurrences of the wavelet magnitude, which makes it difficult to examine the peak amplitude modulation. From Fig. 10, it is clear that only the first peak appears with the absence of other modes. The primary peak exhibits a much lower level of energy, with a slight shift towards the higher frequencies ($St_s = 2$).
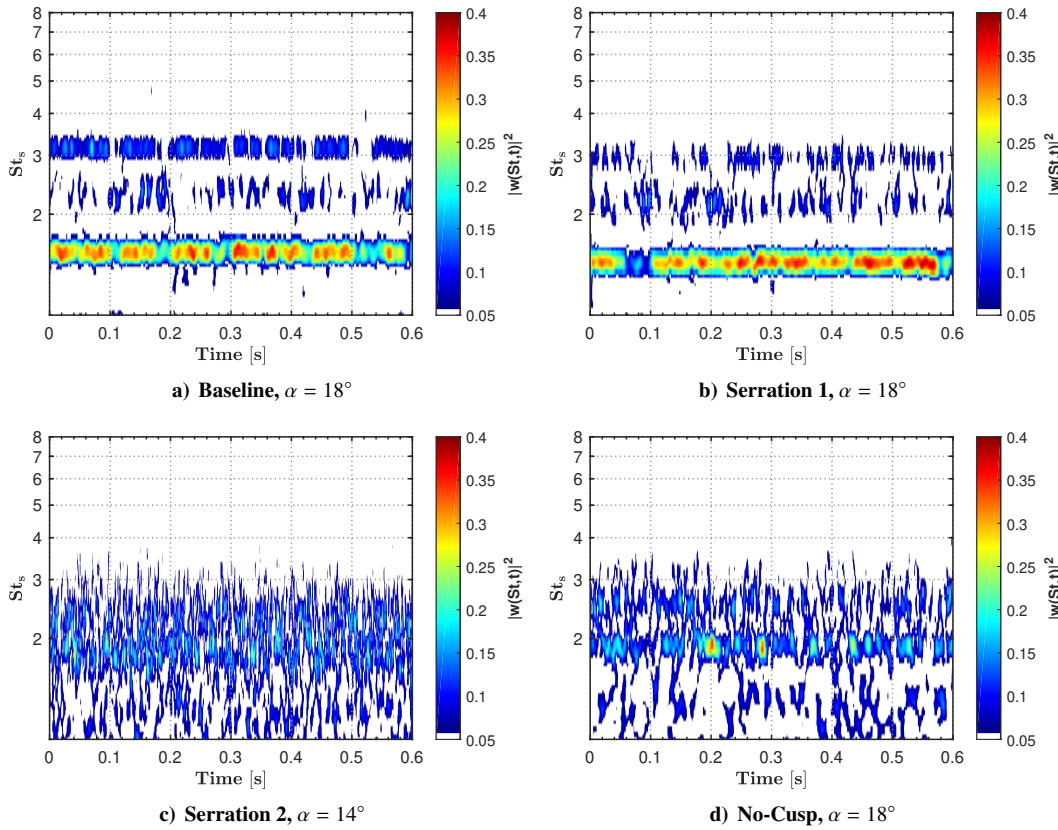

a) **Baseline,** $\alpha = 18°$ b) **Serration 1,** $\alpha = 18°$

c) **Serration 2,** $\alpha = 14°$ d) **No-Cusp,** $\alpha = 18°$

Fig. 10. The contour plots of the wavelet coefficient magnitude for the near-field pressure transducer M1.

F. Auto-bicoherence

The non-linear energy transfer between the frequencies can be studied using the auto-bicoherence (b^2_{ppp} (f_i, f_j) to determine the quadratic and phase coupling between the signal waves. The auto-bicoherence can be calculated using the method employed by Jawahar *et al.* [2, 49]. The contours of the auto-bicoherence for the near-field pressure transducer M1 on the main element at the angle of attack $\alpha = 18°$ for all the configurations are presented in Fig. 11. The results for the Baseline case show that the multiple peaks observed in Fig. 5(b) have quadratic coupled modes due to the self-interaction of the modes in the slat cavity, i.e. $(St_{1.6} - St_{1.6}), (St_{3.2} - St_{3.2}), (St_{4.8} - St_{4.8})$ and $(St_{6.4} - St_{6.4})$., with the corresponding harmonics. Note that the bicoherence value would be $b^2_{ppp} = 1$ if the tonal peak is formed by the non-linear interaction [49]. For the frequency with $St_{4.8}$ and $St_{6.4}$, the bicoherence value is about $b^2_{ppp} > 0.8$, implying that theses harmonics $St_{3.2} = 2St_{1.6}$ and $St_{4.8} = 3St_{1.6}$ could be formed by the quadratic coupling. For the modes at $St_{1.6}$, results have shown the possibility of phase coupling with all the other modes except for St_3, St_4 and

$St_{>8}$. The results also show that the modes between $St_{1.6}$ and $St_{3.2}$ and $St_{3.2}$ and $St_{4.8}$ modes are not in phase with themselves but phase coupled with $St_{3.2}$ and $St_{4.8}$. It can also be seen that the self-interaction is absent in the case of the spectral hump observed in Fig. 5(b), suggesting that the broadband hump is independent and is not quadratically coupled. The bicoherence results for the Ser-1 case show almost similar results with the Baseline case with only a few weak quadratic couple modes. The Ser-2 and No-Cusp cases, on the other hand, show self-interaction of the broadband hump observed in the near-field surface pressure results in Fig. 5(b). A much weaker of self-interaction occurs at about St_2 for both the cases. It can be inferred that both the cases (Ser-2 and No-Cusp) can significantly eliminate the fundamental peak and weaken the constructive self-interaction of the modes compared to the Baseline case.
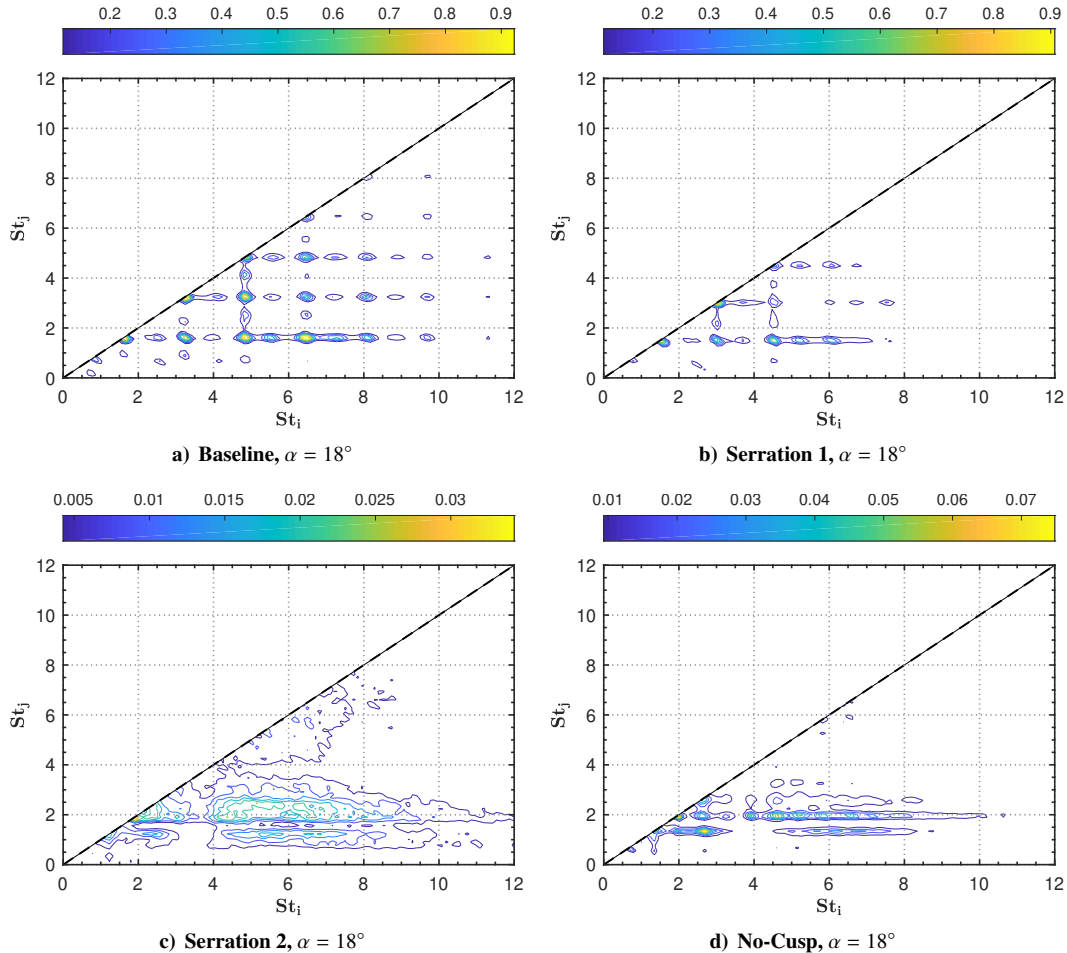

Fig. 11. The auto-bicoherence contour for transducer M1 on the main element for the angle of attack $\alpha = 18°$ for all cases.

G. Persistence spectrum

To further understand the nature of the multiple distinct peaks observed in the present study, the phase coupling and interference of the signals were analyzed using the persistence spectrum. For this purpose, the signals obtained by the transducer M1 on the main element of the airfoil is used to plot the persistence spectrum. The measurement was carried out for 16 s, with a time resolution of 0.04 s and frequency resolution of $St_s = 0.45$ using the Short-Time Fourier Transform (STFF). The contour plot of the persistence spectrum for all the configurations at the angle of attack of $\alpha = 18°$ is presented in Fig. 12. For the Baseline and Ser-1 cases, it can be observed that the primary acoustic energy is present throughout the whole time at the vortex shedding frequency ($St_s = 1.6$). The harmonics of the vortex shedding peak ($St_s = 3.2$ and $St_s = 4.8$) displays the maximum highest energy content over the time period. A much lesser energy level distributed over time can be observed for the peak at odd St_s number. The odd modes do not have any phase relation with the even modes, as can be seen in the auto-bicoherence results in Fig. 11. As anticipated, the results for the Ser-2 and No-Cusp configurations show that the pressure signal is of broadband nature over the entire

time period. It can also be seen that the emergence of the broadband spectral hump observed in Fig. 5(b) for all cases tested is not dominated over the time period.
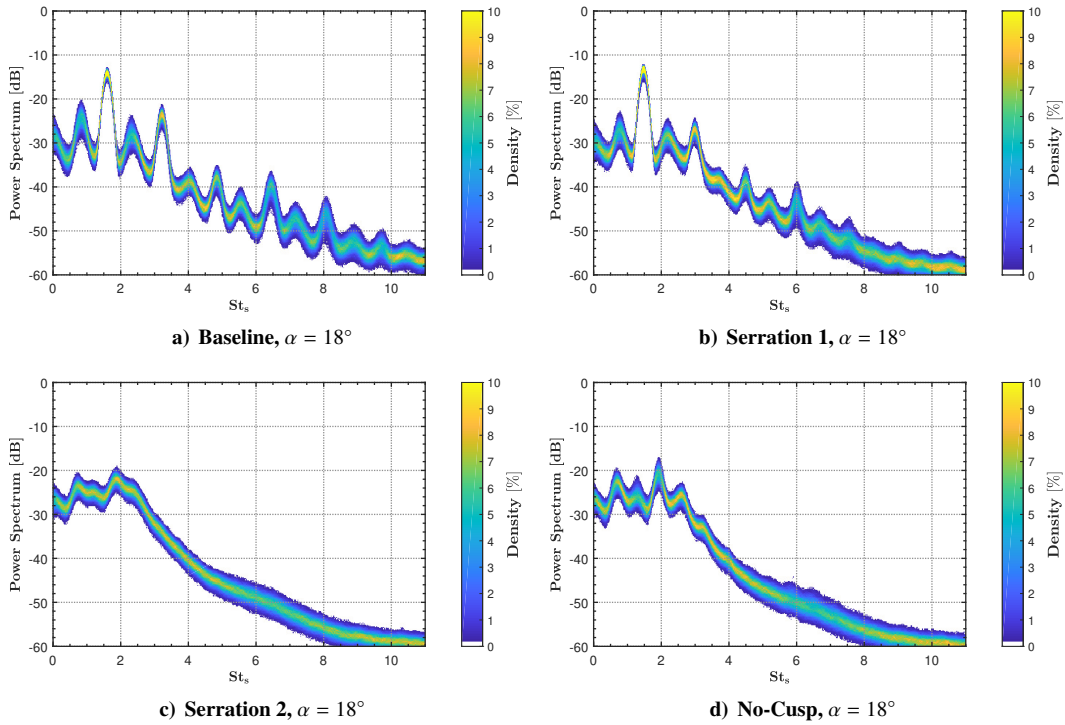

a) Baseline, $\alpha = 18°$

b) Serration 1, $\alpha = 18°$

c) Serration 2, $\alpha = 18°$

d) No-Cusp, $\alpha = 18°$

Fig. 12. The persistence spectrum contour for the near-field pressure transducer M1 on the main element angle of attack $\alpha = 18°$.

H. Correlation studies

The cross-correlation were calculated using the unsteady surface pressure, it is defined as,

$$R_{p_i p_j}(\tau) = \frac{\overline{p_i(t + \tau)p_j(t)}}{p_{i_{rms}}p_{j_{rms}}}, \quad \text{for } p_i = \text{M1 and } p_j = \text{M1, M2, M3, M4,} \tag{2}$$

where p_i and $p_{i_{rms}}$ are the surface pressure and surface pressure root mean squared of the reference transducer signal (M1), p_j and $p_{j_{rms}}$ are the surface pressure and surface pressure root mean squared of the transducer signals at various location along the chord, τ is the time delay and the time average is represented by the overbar.

The results of the cross-correlation of the surface pressure between the reference transducer M1 and transducers M1-M4 for the Baseline, Ser-1, Ser-2, and No-Cusp configurations at the angle of attack 14° and 18° are presented in Fig. 13. The $R_{p_i p_j}(\tau)$ results generally show that as the separation distance between the transducers increases, the time-delay of the peak value in the cross-correlation increases. For the Baseline and Ser-1 cases, a slow decaying periodic behavior with Gaussian shape is observed at both the angles of attack (14° and 18°), which indicates the emanation of a strong vortex shedding. The distance between the two peaks in $R_{p_i p_j}(\tau)$ results for the Baseline case in both of the presented angles of attack corresponds to the vortex shedding frequency. Note that the calculated time delay for the two peaks in the Baseline case is $\tau \approx 0.625$, which corresponds to $St_s = 1.6$, which is the fundamental vortex shedding peak with the highest magnitude. The $R_{p_i p_j}(\tau)$ results of the Ser-2 and No-Cusp cases show a very weak periodic shape that exhibits a fast decaying periodic behavior, signifying the absence of a strong vortex shedding for the angle of attack 14°, which is in agreement with the results observed in Figs. 5 , 6 and 8.
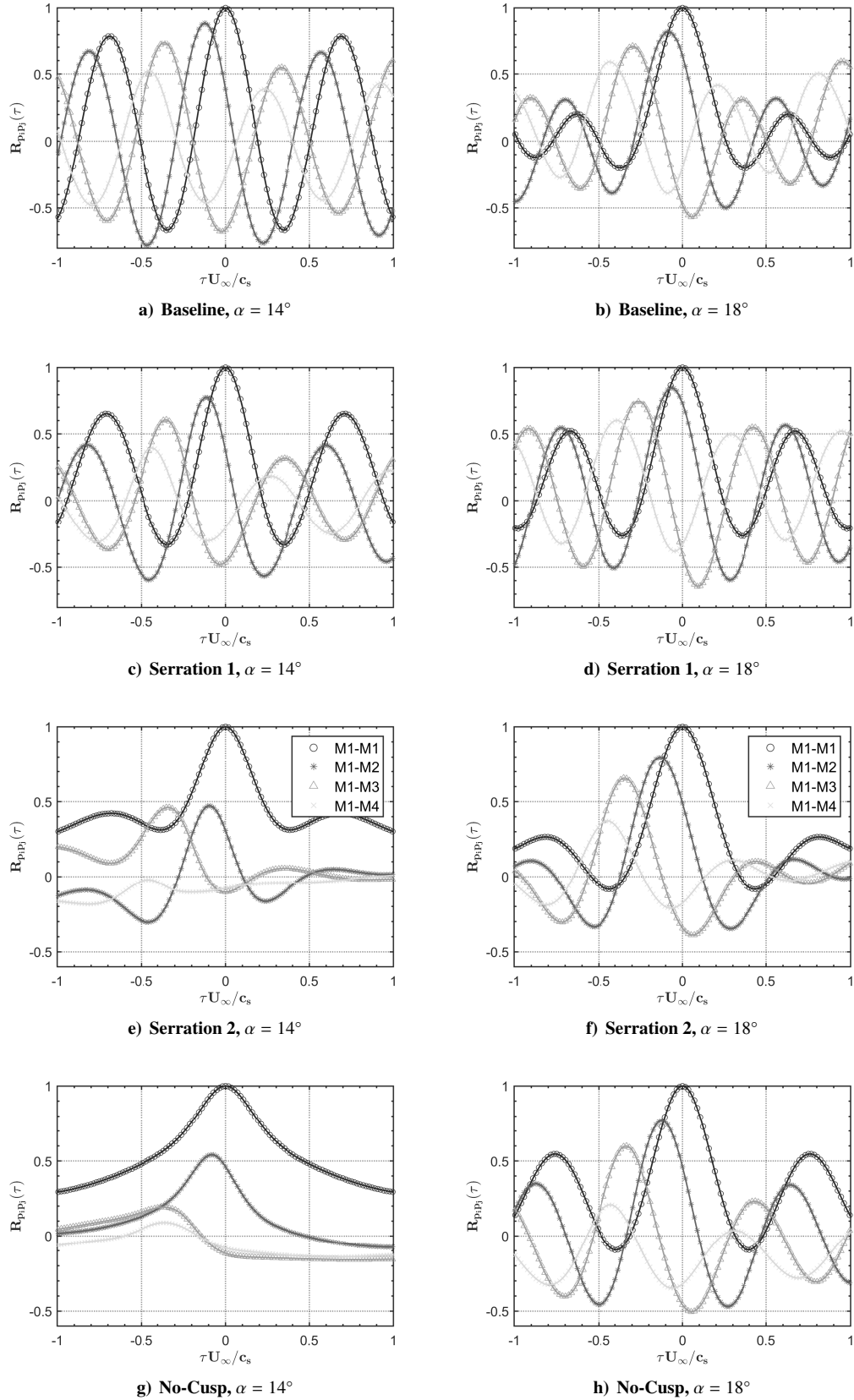
a) **Baseline,** $\alpha = 14°$

b) **Baseline,** $\alpha = 18°$

c) **Serration 1,** $\alpha = 14°$

d) **Serration 1,** $\alpha = 18°$

e) **Serration 2,** $\alpha = 14°$

f) **Serration 2,** $\alpha = 18°$

g) **No-Cusp,** $\alpha = 14°$

h) **No-Cusp,** $\alpha = 18°$

Fig. 13. Cross-correlation between the surface pressure transducers on the main-element with M1 as the reference signal.

American Institute of Aeronautics and Astronautics

IV. Conclusion

The aeroacoustic study of a 30P30N airfoil fitted with two types of serrated slat cusps was studied extensively. The airfoil was equipped with several surface mounted unsteady surface pressure measurement probes around the slat region to isolate the noise sources. The near-field and far-field results show significant noise reduction for Serration-2 configuration. However, no noise reduction is observed for Serration-1 configuration but a mild reduction in the narrowband peak energy was observed. The results for the Serration-2 case also show that the spectral hump observed in the Baseline case has been completely eliminated. The coherence of the broadband hump, the vortex shedding peak, and the other distinct narrowband peaks observed in the Baseline case can be completely eliminated with the No-Cusp configuration. The results of the wavelet coefficient show that the spectral peaks for the Baseline case are the amplitudes modulated in time and that these peaks are absent in the case of Serration-2 and No-Cusp configurations. The results have also shown that the peaks observed in the Baseline case exhibit quadratic self-interaction in the slat cavity. This paper shows that the application of Serration-2 and No-Cusp can significantly reduce the peaks formed by the slat cavity and the broadband noise.

References

[1] Kamliya Jawahar, H., Theunissen, R., Azarpeyvand, M., and Carlos R.Ilario., "Flow characteristics of slat cove fillers", *Aerospace Science and Technology*, Vol. 100, 2020, 105789.

[2] Kamliya Jawahar, H., Showkat Ali, S. A., Azarpeyvand, M., and Ilario, C., "Aerodynamic and aeroacoustic performance of high-lift airfoil fitted with slat cove fillers", *Journal of Sound and Vibration*, Vol. 479, 2020, 115347.

[3] Kamliya Jawahar, H., Azarpeyvand, M., and Carlos R.Ilario., "Aerodynamic and Aeroacoustic Performance of Three-element High Lift Airfoil fitted with Various Cove Fillers", AIAA 2018-3142, 2018.

[4] Kamliya Jawahar, H., Showkat Ali, S. A., Azarpeyvand, M., and Carlos R.Ilario., "Aeroacoustic Performance of Three-element High Lift Airfoil with Slat Cove Fillers", AIAA 2019-2440, 2019.

[5] Kamliya Jawahar, H., Azarpeyvand, M., and Carlos R.Ilario. "Experimental Investigation of Flow Around Three-element High-lift Airfoil with Morphing Fillers", AIAA 2017-3364, 2017.

[6] Kamliya Jawahar, H., Ai, Q., and Azarpeyvand, M., "Experimental and Numerical Investigation of Aerodynamic Performance of Airfoils with Morphed Trailing Edges", *Renewable Energy*, Vol. 127, 2018, pp. 355-367.

[7] Showkat Ali, S. A., Azarpeyvand, M., and Ilario, C., "Trailing Edge Flow and Noise Control using Porous Treatments", *Journal of Fluid Mechanics*, Vol. 850, 2018, pp. 83-119.

[8] Showkat Ali, S. A., Azarpeyvand, M., Szoke, M. and da Silva, C. R. I., "Boundary layer flow interaction with a permeable wall," *Physics of Fluids*, Vol. 30, 2018, pp. 085111.

[9] Showkat Ali, S. A., Azarpeyvand, M. and da Silva, C. R. I., "Trailing edge bluntness noise reduction using porous treatments," *Journal of Sound and Vibration*, Vol. 474, 2020, pp. 115257.

[10] Showkat Ali, S. A., Szoke, M., Azarpeyvand, M., and Ilario, C., "Turbulent Flow Interaction with Porous Surfaces", AIAA 2018-2801, 2018.

[11] Showkat Ali, S. A., Liu, X., and Azarpeyvand, M., "Bluff body flow and noise control using porous media", AIAA 2016-2754, 2016.

[12] Celik, A., Mayer, Y. D., and Azarpeyvand, M., "An experimental aeroacoustic study on serrated trailing-edge geometries and flow misalignment effects", 26th AIAA/CEAS Aeroacoustics Conference, 2020.

[13] Celik, A., Bowen, L., and Azarpeyvand, M., "Effects of trailing edge bevel angle on the sound generation of a flat plate", 26th AIAA/CEAS Aeroacoustics Conference, 2020.

[14] Celik, A., and Azarpeyvand, M., "Effect of adverse and favorable pressure gradient on hydrodynamic field of a serrated flat plate", 26th AIAA/CEAS Aeroacoustics Conference, 2020.

[15] Liu, X., Kamliya Jawahar, H., Azarpeyvand, M., and Theunissen, R., "Aerodynamic Performance and Wake Development of Airfoils with Serrated Trailing Edges", *AIAA Journal*, Vol. 55, No. 11, 2017, pp. 3669-3680.

[16] Liu, X., Showkat Ali, S. A., Azarpeyvand, M., and Theunissen, R., "On the Application of Trailing-edge Serrations for Noise Control from Tandem Airfoil Configurations", AIAA 2017-3716, 2017.

[17] Lyu, B., Azarpeyvand, M., and Sinayoko, S., "Prediction of Noise from Serrated Trailing Edges", *Journal of Fluid Mechanics*, Vol. 793, 2016, pp. 556-588.

[18] Mayer, Y. D., Lyu, B., Kamliya Jawahar, H., and Azarpeyvand, M., "A Semi-analytical Noise Prediction Model for Airfoils with Serrated trailing-edges", *Renewable Energy*, Vol. 143, 2019, 679–691.

[19] Roger, M., and Perennes, S., "Low-Frequency Noise Source in Two Dimensional High-lift Devices", AIAA 2000-1972, 2000.

[20] Kolb, A., Faulhaber, P., Drobietz, R., and Grunewald, M., "Aeroacoustic Wind Turbine Measurements on a 2D High-lift Configuration", AIAA 2007-3447, 2007.

[21] Mendoza, J.M., Brooks, T.F., and Humphreys, W.M., "An Aeroacoustic Study of a leading-edge Slat Configuration", *international Journal of Aeroacoustics*, Vol. 1, No. 3, 2002, pp. 241-274.

[22] Hein, S., Hohage, T., Koch, W., and Schoberl, J., "Acoustic Resonances in a High-lift Configuration", *Journal of Fluid Mechanics*, Vol. 582, pp: 179-202, 2007.

[23] Makiya, Sanehiro., Inasawa, A., and Asai, M., "Vortex Shedding and Noise Radiation from a Slat Trailing Edge", *AIAA Journal*, Vol. 48, No. 2, 2010, pp: 502-508.

[24] Terracol, M., Manoha, E., and Lemoine, B., "Investigation of the Unsteady Flow and Noise Generation in a Slat Cove", *AIAA Journal*, Vol. 54, No. 2, 2016, pp: 469-489.

[25] Pagani, C. C., Souza, D. S., and Medeiros, M. F., "Slat Noise: Aeroacoustic Beamforming in Closed-Section Wind Tunnel with Numerical Comparison", *AIAA Journal*, Vol. 54, No. 7, 2016, pp: 2100-2115.

[26] Pagani, C. C., Souza, D. S., and Medeiros, M. F., "Experimental Investigation on the Effect of Slat Geometrical Configuration on Aerodynamic Noise", *Journal of Sound and Vibration*, Vol. 394, pp: 256-279, 2017.

[27] Pascioni, K. A., and Cattafesta, L. N., "An Aeroacoustic Study of a Leading-edge Slat: Beamforming and Far-field Estimation using Near-field Quantities", *Journal of Sound and Vibration*, Vol. 429, pp: 224-244, 2018.

[28] Li, L., Liu, P., Guo, H., Hou, Y., Geng, X., and Wang, J., "Aeroacoustic Measurement of 30P30N High-lift Configuration in the Test Section with Kevlar Cloth and Perforated Plate", *Aerospace Science and Technology*, Vol. 70, pp: 590-599, 2017.

[29] Li, L., Liu, P., Guo, H., Geng, X., Hou, Y., and Wang, J., "Aerodynamic and Aeroacoustic Experimental Investigation of 30P30N High-lift Configuration", *Applied Acoustics*, Vol. 132, pp: 43-48, 2018.

[30] Li, L., Liu, P., Xing, Y., and Guo, H., "Time-frequency Analysis of Acoustic Signals from a High-lift Configuration with two Wavelet Functions", *Applied Acoustics*, Vol. 129, pp: 155-160, 2018.

[31] Li, L., Liu, P., Xing, Y., and Guo, H., "Wavelet Analysis of the Far-Field Sound Pressure Signals Generated from a High-lift Configuration", *AIAA Journal*, Vol. 56, No. 1 pp: 432-437, 2018.

[32] Li, y., Wang, X., and Zhang, D., "Control strategies for aircraft airframe noise reduction", *Chinese Journal of Aeronautics*, Vol. 26, No. 2 pp: 249-260, 2013.

[33] Horne, W. C., James, K. D., Arledge, T. K., Soderman, P. T., Field, M., Burnside, N., and Jaeger, S. M., "Measurement of 26%-scale 777 Airframe Noise in the NASA Ames 40- by 80 foot Wind Tunnel", AIAA 2005-2810, 2005.

[34] Streett, C., Casper, J., Lockard, D., Khorrami, M., Stoker, R., Elkoby, R., Wenneman, W., and Underbrink, J., "Aerodynamic Noise Reduction for High-Lift Devices on a Swept Wing Model", AIAA 2006-212, 2006.

[35] Andreou, C., Graham, W., Shin, H.C., Street, T., Member, S., and Lecturer, S., "Aeroacoustic study of airfoil leading-edge high-lift devices", AIAA 2006-2515, 2006.

[36] Andreou, C., Graham, W., Shin, H.-c., Introduction, I., Street, T., Member, S., and Lecturer, S., "Aeroacoustic Comparison of Airfoil leading-edge High-Lift Geometries and Supports", AIAA 2007-230, 2007.

[37] Murayama, M., Nakakita, K., Yamamoto, K., Ura, H., and Ito, Y., "Experimental Study of Slat Noise from 30P30N Three-Element High-Lift Airfoil in JAXA Hard-Wall Low-Speed Wind Tunnel", AIAA 2014-2080, 2014.

[38] Imamura, T., Ura, H., Yokokawa, Y., Enomoto, S., Yamamoto, K., Hirai, T., Group, A. P., and Division, E. S., "Designing of Slat Cove Filler as a Noise Reduction Device for Leading-edge Slat", AIAA 2007-3473, 2007.

[39] Ura, H., Yokokawa, Y., Imamura, T., Ito, T., and Yamamoto, K., "Investigation of Airframe Noise from High Lift Configuration Model", AIAA 2008-19, 2008.

[40] Shmilovich, A., Yadlin, Y., and Pitera, D. M., "Wing leading-edge Concepts for Noise Reduction", 27th International Congress of the Aeronautical Sciences (ICAS), 2010.

[41] Shmilovich, A., Yadlin, Y., and Company, T. B., "High-lift systems for enhanced take-off performance", 28th International Congress of the Aeronautical Sciences, 2012, pp. 1-13.

[42] Scholten, W. D., Hartl, D. J., Turner, T. L., and Kidd, R. T., "Development and Analysis-Driven Optimization of Superelastic Slat-Cove Fillers for Airframe Noise Reduction", *AIAA Journal*, dec 2015, pp. 1-17.

[43] Tao, J. and Sun, G., "A Novel Optimization Method for Maintaining Aerodynamic Performances in Noise Reduction Design", Aerospace Science and Technology, Vol. 43, 2015, pp. 415-422.

[44] Kopiev, V. M., Zaitsev, Y. M., Belyaev, I. V., and Mironov, M. A., "Noise Reduction Potential through Slat Hook Serrations", AIAA 2011-2909, 2011.

[45] Mayer, Y., Kamliya Jawahar, H., Mate, S., Showkat Ali. S.A., and Azarpeyvand, M., "Design and performance of an aeroacoustic wind tunnel facility at the University of Bristol", *Applied Acoustics*, Vol. 155, 2019, pp. 358-370.

[46] Garcia-Sagrado, A. and Hynes, T., "Wall-Pressure Sources Near an Airfoil Trailing Edge Under Separated Laminar Boundary Layers", *AIAA Journal*, Vol. 49, No. 9, 2011, pp. 1841-1856.

[47] Garcia-Sagrado, A. and Hynes, T., "Stochastic Estimation of Flow near the Trailing Edge of a NACA0012 Airfoil", *Experiments in Fluids*, Vol. 51, No. 4, 2011, pp. 1057-1071.

[48] Garcia-Sagrado, A. and Hynes, T., "Wall Pressure Sources Near an Airfoil Trailing Edge under Turbulent Boundary Layers", *Journal of Fluids and Structures*, Vol. 30, 2012, pp. 3-34.

[49] Mallat, S., "A Wavelet Tour of Signal Processing", Academic, New York, 1998.